The competition for graphene formation on Re(0001): a complex interplay between carbon segregation, dissolution and carburization

E. Miniussi[a,b], M. Pozzo[c], T.O. Menteş[d], M.A. Niño[e], A. Locatelli[d], E. Vesselli[a,b], G. Comelli[a,b], S. Lizzit[d], D. Alfè[c,f], A. Baraldi[a,b,*]

[a] *Physics Department and CENMAT, University of Trieste, Via Valerio 2, 34127 Trieste, Italy*
[b] *IOM-CNR, Laboratorio TASC, S.S. 14 Km 163.5, 34149 Trieste, Italy*
[c] *Department of Earth Sciences, Department of Physics and Astronomy, Thomas Young Centre@UCL, and London Centre for Nanotechnology, University College London, Gower Street, London WC1E 6BT, United Kingdom*
[d] *Elettra - Sincrotrone Trieste S.C.p.A., S.S. 14 Km 163.5, 34149 Trieste, ITALY*
[e] *Instituto Madrileño de Estudios Avanzados en Nanociencia (IMDEA Nanociencia), Cantoblanco, 28049 Madrid, Spain*
[f] *IOM-CNR, DEMOCRITOS National Simulation Centre, 34100 Trieste, Italy*

Abstract

We study the interplay between competitive substrate-C interaction processes occurring during chemical vapour deposition (CVD) of ethylene on Re(0001). At T $<$ 500 K dissociative ethylene adsorption leads to the formation of a dimer species, producing an ordered (4 $\times$ 2) structure. In the range 500 $-$ 700 K, the formation of a high–quality single–layer of graphene (GR) is strongly opposed by the formation of a surface carbide characterised by C trimer units, and, at higher temperatures, by carbon dissolution into the bulk. Our experimental and theoretical results demonstrate that, under UHV conditions, the formation of a long-range ordered GR layer on

*Corresponding author. Tel.(+39)040 375-8719. E-mail:alessandro.baraldi@elettra.eu

Re(0001) without carbon bulk saturation is confined to a narrow window of growth parameters: substrate temperature, hydrocarbon gas pressure and exposure time. Our combined experimental and theoretical approach allowed us to validate a concept which had already been anticipated in some earlier works on Rh,Fe and Ni, namely that the epitaxial growth of GR is not necessarily restricted to surfaces where carburisation is precluded, but could take place, under given appropriate conditions, also on other metallic substrates exhibiting a strong C-substrate interaction.

Keywords:

---

1. Introduction

In order to develop graphene (GR)–based technologies, a key issue to tackle is the large scale production of high quality GR in an easily controllable and reproducible way. Among the various methods so far proposed [1], chemical vapour deposition (CVD) on metal surfaces is one of the most promising routes [2–4]. However, there are still quite a few limitations to the industrial employment of this process, which is energetically very demanding, due to the need of cracking the hydrocarbon molecules contained in the commonly used gas mixtures, such as C_2H_4+H_2, on copper and nickel surfaces at relatively high temperatures (T$\simeq$1250 K) [5, 6].

In this respect, one of the primary goals of the scientific community is understanding the atomic–scale mechanism responsible for GR formation and its interaction with the substrate, in order to achieve a better control over the CVD conditions and to ultimately improve the quality of the GR sheets so obtained.

In order to reach this goal, several obstacles need to be overcome. On one hand, low sample temperatures during deposition ($T \lesssim 900\,K$) may inhibit the complete dissociation of hydrocarbon molecules and lead to the formation of GR layers with a high density of vacancies and/or domain boundaries. The presence of these defects significantly modifies the transport properties of GR. On the other hand, high temperatures, combined with particular pressure conditions, can lead to the formation of surface carbides and/or to the penetration of C atoms in the bulk of the solid.

The present work focuses on three exemplary competing processes governed by the interaction between C atoms and the substrate: GR growth, surface carbide formation and C dissolution into the bulk. Several studies have pointed out that the interaction of carbon atoms with the metal substrate can significantly change from one surface to another, resulting in the formation of either chemisorbed carbon, surface carbides or GR [7, 8]. Moreover, it is widely accepted that GR itself can develop different types of interaction with transition metal surfaces, ranging from weak physisorption to strong coupling, which strongly affects the transport properties and thermal stability of the carbon layers [2, 9]. In this respect, substrates like Ir(111) [10–12] and Pt(111) [13–17] appear especially attractive because of the weak interaction they develop with the C layer, which allows preserving most of the exceptional properties of free standing GR. In the specific case of Pt(111), extended, uniform GR sheets can be synthesised not only by CVD [13–16], but also by C surface precipitation from the C-doped bulk [17–20].

In this context, the case of GR/Re(0001) deserves particular attention,

because on this substrate GR growth is energetically nearly as favourable as surface carbide formation [7].

Some earlier studies conducted by Gall *et al.* [21] on polycrystalline Rhenium had already highlighted the possibility of growing 2–dimensional graphitic carbon layers on this metal; the experimental methods which were employed, though, did not enable a thorough understanding of the mechanisms involved in the formation of GR and other carbon species. In our work, we introduced an advanced, innovative approach based on the combination of experimental spectroscopy, diffraction and microscopy techniques and state–of–the–art DFT calculations, to characterise the growth of GR and other carbon species on Re(0001) and develop a consistent interpretation of the data. In contrast with what reported in previous works, we found that there is no actual need to saturate the bulk of the substrate with carbon to achieve GR formation, and that in these conditions (i.e. when the bulk is not saturated with carbon) the optimum GR growth temperature is significantly lower than previously believed. Furthermore, under specific pressure and temperature growth conditions, we observe a complex, competitive interplay among different carbon species (chemisorbed carbon, surface carbides, bulk dissolved carbon and, indeed, GR), which had not been reported before for other systems.

2. Experimental

The measurements were carried out in three different experimental systems. The preliminary characterization of the C phases formed on Re(0001) upon C_2H_4 thermal decomposition was carried out in the ultra–high vacuum

chamber of the Surface Science Laboratory at Elettra - Sincrotrone Trieste, which, besides the standard sample cleaning facilities, is equipped with x–ray sources and with a hemispherical electron energy analyser. The experimental set–up also includes a Low Energy Electron Diffraction (LEED) optics system and a quadrupole mass spectrometer, which was used for the Thermal Desorption Spectroscopy (TDS) experiments described in the following. The sample is supported by a very thin Ta wire directly spotwelded on the back of the crystal (no sample holder is used); this mounting allows heating the crystal either by radiation or by electron bombardment.

The high energy resolution photoelectron spectroscopy experiments were performed at the SuperESCA beam line [22] of the Elettra synchrotron radiation facility. The photoemission spectra were collected by a SPECS Phoibos 150 mm mean radius hemispherical electron energy analyzer equipped with a home-made delay line detection system. The experimental set–up combines high energy resolution with fast data acquisition rates, which enabled us to monitor during C_2H_4 deposition the time evolution of the C $1s$ and Re $4f_{7/2}$ core levels over a wide temperature range. The overall experimental energy resolution (taking into account both the electron energy analyser and the photon beam) was about 40 meV for all measurements. In this case the Re(0001) sample was mounted on a manipulator with four degrees of freedom. The sample was cooled by liquid nitrogen and heated by electron bombardment from the back, and its temperature was monitored by means of a W−Re thermocouple spot–welded on one side of the sample. The experimental chamber is equipped also with a rear view LEED optics, a gas inlet system and a mass spectrometer.

The microscopy experiments were carried out at the Nanospectroscopy beam line at Elettra, which is equipped with a spectroscopy and low energy electron microscope [23, 24] (SPELEEM). Low Energy Electron Microscopy (LEEM) is a full–field microscopy technique which allows collecting either an image or a LEED pattern of the surface, thus gaining access to complementary information in real and reciprocal space [23, 25, 26]. With this system, it is also possible to acquire the micro–spot LEED ($\mu-$LEED) pattern from a restricted region of the sample (between 2 and 10 µm wide)[1]. The experimental chamber of the Nanospectroscopy beam line is equipped also with standard facilities for sample cleaning and preparation. The temperature of the Re(0001) sample during the experiments was monitored both by an infra–red pyrometer and a C-type thermocouple in contact with the sample holder.

In all three experimental systems, the Re(0001) surface was cleaned by cycles of Ar^+ sputtering at 2.5 keV and repeated oxidizing treatments ($p_{O_2}=2 \times 10^{-7}$ mbar), followed by annealing to 2000 K.

The acquired XPS spectra were fitted to Doniach-Šunjič (DS) functions [27] convoluted with a Gaussian distribution. The DS profile includes a Lorentzian width Γ, which accounts for the finite core–hole lifetime, and a singularity index α, to describe the asymmetric shape of the spectra arising from core–hole screening effects. The vibrational fine structure, along with any instrumental or inhomogeneous broadening, contributes to the Gaussian width G. The background was assumed to be linear. The binding energies (BEs) of the

[1]See Supplementary Data

core level components are all referred to the Fermi level, measured under the same experimental conditions.

The C coverage corresponding to each carbon phase was estimated by comparing the integrated intensity of the related C 1s core level photoemission signal with that of GR. As explained in detail later on, single–layer GR on Re(0001) corresponds to a C coverage of 2.47 ML, as determined from the experimental data. In order to mediate possible photoelectron diffraction effects, our comparison was not restricted to photoemission spectra acquired at a single photon energy, but multiple data sets collected at photon energies in the range $350 \div 550$ eV were considered.

Calculations were performed using Density Functional Theory, [28, 29] with exchange-correlation effects included at the level of the PBE-GGA [30] functional. We used the Projector Augmented Wave [31] (PAW) method as implemented in VASP [32, 33] to account for the core electrons of both Re and C atoms, with the 6s and 5d electrons of Re and the 2s and 2p electrons of C explicitly included in the valence. We used a plane–wave kinetic energy cutoff of 400 eV. The (0001) surface of Re was modelled using a slab with a thickness of 4 layers, with the atoms of the 2 bottom layers kept fixed at their bulk positions, while all the other atoms were allowed to relax. A vacuum interspace of at least 10 Å was used to minimize the interaction between periodic images of the slab along the direction perpendicular to the surface, resulting in a super–cell of 25 Å along the z axis.

Core-level BEs for both C and Re atoms have been estimated in the so-called final-state approximation. This estimate does not include the effect of core-electron screening, as the other core electrons remain fixed at the

electronic configurations used to generate the PAW potential. However the screening from valence electrons is included, thus providing an accurate estimate of its effect on the core level BE. Although the absolute core level energies are not directly accessible because of the frozen core approximation, differences of core level energies are usually accurately reproduced [34]. The Surface Core Level Shifts (SCLS) are then given as the difference of core electron binding energies E_b between the surface and bulk Re atoms, i.e.

$$SCLS = E_b(\text{Surf}) - E_b(\text{Bulk}). \quad (1)$$

In order to correctly take into account the final state contribution in the case of Re, core electrons from the $4f$ shell have been excited to the lowest empty band. According to previous theoretical studies [34], the method used in the present work calculates the SCLSs with an accuracy of about $20 - 50$ meV.

3. Results and Discussion

3.1. Low temperature carbon overlayers

All the distinct carbon phases described in this work were obtained on Re(0001) by exposing the sample to a flux of ethylene (C_2H_4) molecules under different temperature and pressure conditions.

In the first part of our investigation, we determined the temperature above which ethylene dissociation into C and H is complete. To this purpose, we carried out a series of TDS experiments, in which the sample was first exposed to C_2H_4 at T=170 K and subsequently annealed to 800 K using a linear rate of $2\,\mathrm{K\,s^{-1}}$. In order to prevent spurious contributions to the

TD spectrum due to hydrogen desorption from the W filaments, before each experiment we flash-annealed the filaments up to the hydrogen desorption temperature while still keeping the sample at low temperature. The head of the mass spectrometer was positioned very close to the sample, a configuration which is commonly adopted in this kind of experiments in order to select the desorption signal from the crystal without collecting spurious contributions from the background.

The desorption signals of H_2 ($m/e = 2$), of molecular C_2H_4 ($m/e = 28$), and of the various species produced by C_2H_4 fragmentation ($m/e = 16$, 26, 27), were monitored as a function of the temperature for different initial exposures. An accurate calibration of the sample coverage as a function of the exposure was made possible by the photoemission experiments (later described). The XPS measurements, in fact, showed that the C coverage at saturation (above 5 L) is about 0.6 ML; therefore, since in a C_2H_4 molecule the stoichiometric C:H ratio is 1 : 2, the H coverage at saturation must be 1.2 ML. From this reference value, we were able to calibrate the H coverage as a function of the exposure by calculating the area of the H_2 desorption curves (after background subtraction) in each TDS experiment.

Since in C_2H_4 the H/C ratio is 2, the corresponding amount of H equals a coverage of about 1.2 ML. The large H_2 desorption signal at $\sim$300 K (Fig. 1), which is not accompanied by an appreciable desorption of other species, suggests that C_2H_4 undergoes a first dehydrogenation already below room temperature.

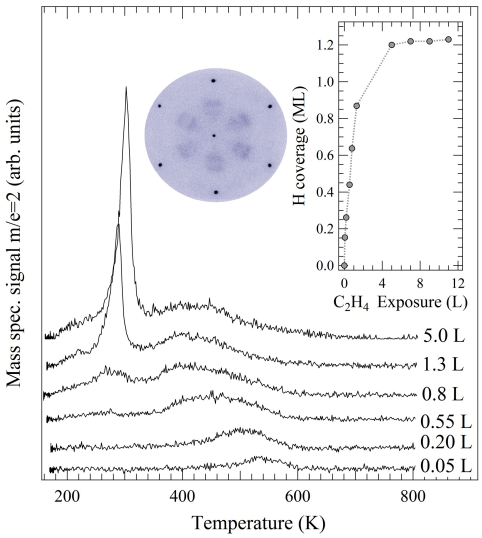

Figure 1: Thermal Desorption spectra of H_2 ($m/e = 2$) for different values of the ethylene exposure at T=170 K. Heating rate =2 K s^{-1}. In the insets are reported the disordered (1×1) LEED pattern of the Re(0001) surface after C_2H_4 adsorption at room temperature and (on the right) the experimentally determined H uptake curve.

This is in agreement with an earlier work on C_2H_4 adsorption on polycrystalline Re and on Re(0001) by Ducros et al. [35], who already observed that the thermal desorption spectrum after C_2H_4 saturation exposure at room temperature is dominated by the H_2 signal. In the inset of Fig. 1 the evolution of the H surface coverage is shown as a function of the initial C_2H_4 exposure; it is clear that saturation is reached after a C_2H_4 exposure between 2 and 5 L.

At room temperature, C_2H_4 adsorption on Re(0001) results in the formation of a disordered adlayer. This surface is characterised by a LEED pattern exhibiting a (1×1) periodicity with an intense background and diffuse diffraction maxima along the direction between the $(0, 0)$ and the first-order spots

of the substrate (see inset in Fig. 1). Annealing of the C_2H_4-saturated substrate to T$\sim$750 K, a temperature at which we know that only atomic C is present on the surface (see below), leads to the appearance of a LEED pattern with $c(4 \times 2)$ periodicity (Fig. 2(a)). This diffraction pattern, which had already been reported by Ducros et al. [35] under similar experimental conditions, results from the superposition of three non–equivalent rotational domains oriented at 120° from one another.

Our LEED experiments proved that the highest quality $c(4 \times 2)$ overlayer is formed by C_2H_4 exposure at 750 K. This conclusion was drawn from the analysis of the intensity and Lorentzian full width at half maximum (FWHM) of the overlayer diffraction spots as a function of the C_2H_4 exposure. The spots not only gain intensity, but also become sharper, which indicates that a long–range order has been achieved in the overlayer [2]. A maximum in the intensity, and a corresponding minimum in the Lorentzian width of the diffraction spots, is observed around 2 L exposure. Higher C_2H_4 exposures yield a slow monotonic decrease of the $c(4 \times 2)$ LEED spot intensity, along with a slightly increased Lorentzian broadening: this behaviour suggests that some excess carbon is building up on the surface in a disordered way.

The C 1s core level spectrum of this structure presents a component centred at 283.4 eV, which suggests that all C adatoms in the $c(4 \times 2)$ structure are characterised by a similar adsorption configuration.

[2] See Supplementary Data

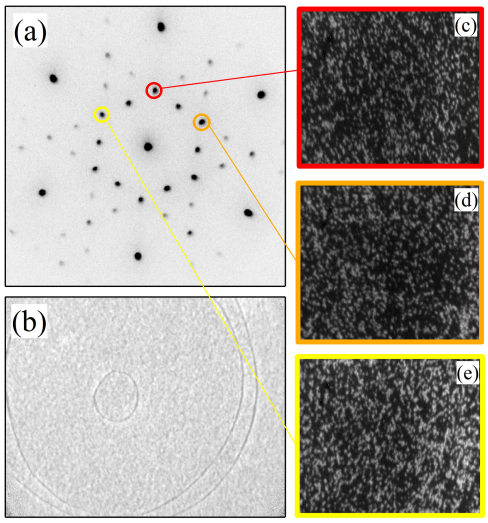

Figure 2: (a) LEED pattern of the $c(4\times2)$ structure ($E = 55$ eV), in which three diffraction spots due to non–equivalent surface domains are differently highlighted. (b) Corresponding bright field image of the surface ($E = 4$ eV, field of view (f.o.v.): 2 µm). (c)–(e) Dark field LEEM images ($E = 16$ eV, f.o.v.: 2 µm) of the three non–equivalent domains corresponding to the LEED spots highlighted in (a).

The presence and distribution of $c(4 \times 2)$ domains on the surface were investigated also by LEEM [23, 25]. Fig. 2(b) shows the corresponding bright field [2](BF) image of the high-quality $c(4 \times 2)$ overlayer, characterised by a non–uniform grey shade, in which the steps and terraces of the Re(0001) substrate can be easily distinguished. The dark field [2] images (Fig. 2 (c-e)) show a high density of small bright grains, indicating the presence of domains with an average size of $\lesssim$20 nm. Moreover, the superposition of the three images corresponding to non–equivalent domains indicates that the ordered layer does not extend over the entire surface: the sum of the bright areas in Fig. 2 (c)–(e), in fact, yields only $80 \pm 10\%$ of the total surface area.

The estimated C coverage of the $c(4 \times 2)$ structure, as obtained from the photoemission data (by comparing the intensity of the C $1s$ signal of this structure with that of GR, as illustrated in the Experimental section), is in the range $0.5 \div 0.75$ ML, thus suggesting an occupation of at least two C atoms per unit cell.

More information on the $c(4\times2)$ structure was obtained from the analysis of the Re $4f_{7/2}$ core level spectra shown in Fig. 3. In a recent experimental and theoretical surface core level (SCL) analysis of clean Re(0001) [36], we identified two core level components (labelled S_b and S_0 in Fig. 3(a)), assigned to photoemission from bulk and surface Re atoms, respectively, with an estimated SCLS of -95 ± 5 meV. The high energy resolution Re $4f_{7/2}$ core level spectra of the $c(4 \times 2)$ structure acquired with a photon energy $h\nu = 200$ eV, at normal and grazing emission, are reported in Fig. 3(b)–(c), respectively.

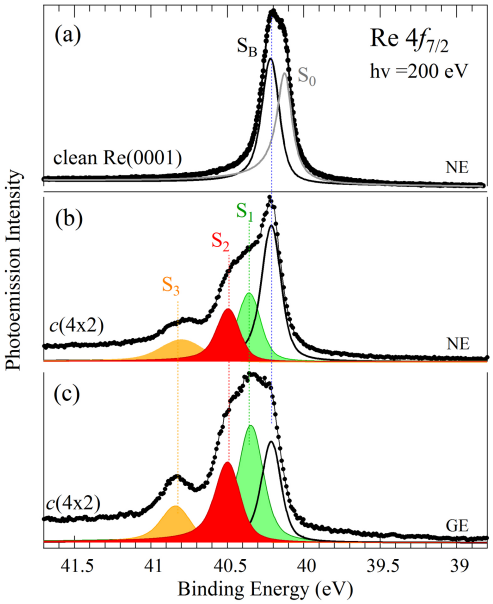

Figure 3: (a) High resolution Re $4f_{7/2}$ core level spectra of clean Re(0001), acquired at normal emission with $h\nu = 200$ eV; the deconvolution into bulk (S_b) and surface (S_0) components is shown superimposed. (b, c) High resolution Re $4f_{7/2}$ core level spectrum of the $c(4\times2)$ structure, collected with $h\nu = 200$ eV, at normal (b) and grazing (c) emission.

As evident by comparing the deconvoluted spectrum of C–covered Re(0001) with that of the clean surface (Fig. 3 (a)), the core level component due to first layer clean surface Re atoms, S_0, is absent in the C–covered spectrum. This reflects a change in the local environment of surface Re atoms, either in terms of new bond formation or in terms of modified local geometry. At the same time, new adsorbate–induced components (labelled S_1–green curve–, S_2–red curve– and S_3–orange curve–in Fig. 3) appear, respectively, at 140 ± 20, 280 ± 25 and 570 ± 25 meV higher BE than the bulk component. The enhanced intensity of these components relative to the bulk peak at grazing emission supports their assignment to surface atoms. Notably,

the S_3 component, besides showing a larger Gaussian width, is considerably less intense than S_1 and S_2: its integrated area at normal emission, in fact, amounts to less than 20% of the combined intensity of the other two components. This suggests that this component could be related, rather than to the ordered $c(4 \times 2)$ structure, to patches of some different carbon species extending on the surface regions left uncovered by the $c(4 \times 2)$, as indicated by the LEEM data.

In order to understand the origin of the various core level components in the Re $4f_{7/2}$ spectrum and to determine the geometry of the $c(4 \times 2)$ structure, we performed a set of DFT calculations at variable C coverage. We simulated C/Re(0001) structures for coverages ranging from 0.5 to 1.5 ML, and for non–equivalent C adsorption configurations, as shown in Fig. 4, which reports the corresponding model cells with $c(4 \times 2)$ (highlighted by a blue mark) or (4×2) periodicity.

Although, in fact, the diffraction pattern exhibits $c(4 \times 2)$ symmetry, we can reasonably assume that the breaking of the central symmetry, e.g. in correspondence of domain walls, may lead to the local appearance of configurations with (4×2) symmetry. For this reason, in our simulations we also tested configurations with (4×2) periodicity, obtained from local modifications of the original geometry, in order to check whether their presence can account for the C $1s$ line shape observed in the photoemission experiments.

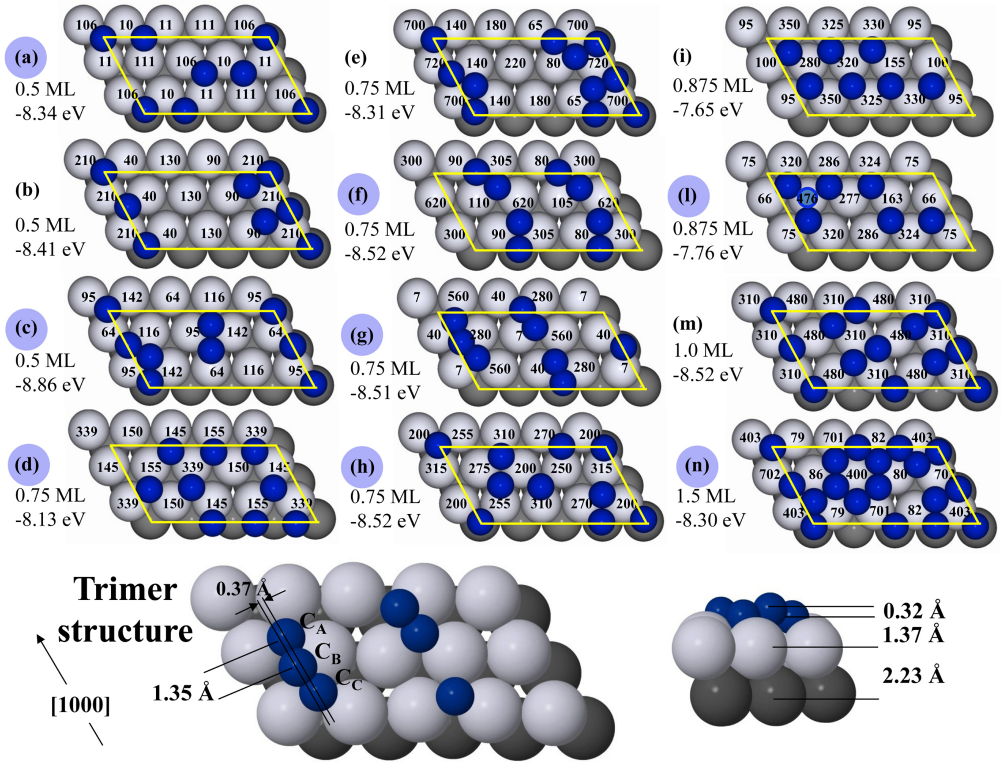

Figure 4: Simulated structural models of C overlayers with coverages between 0.5 and 1.5 ML, assuming C adsorption in different surface sites. The cells with $c(4\times2)$ symmetry are highlighted with a blue mark on the corresponding label; the other structures have (4×2) symmetry. Structure (l) also has a C atom in a subsurface interstitial site, which is indicated by a light blue circle. . For each structure, the C coverage and the total energy are indicated on the left. The values of the calculated SCLSs (in meV) are shown, superimposed to each first-layer Re atom in the different cells. Details of model (g) are highlighted in the bottom panel.

In all the examined configurations, the C atoms occupy fcc or hcp three-fold sites; on–top adsorption was excluded because C atoms on transition metal (TM) surfaces are known to favour high coordination configurations [37]. The configurations with C atoms in bridge sites are found to be metastable,

and tend to relax to three–fold site adsorption. The calculated SCLS corresponding to each first–layer Re atom in the unit cell are also reported in Fig. 4.

As it turns out from our analysis, the most stable configurations are associated with the formation of either dimers or trimers, while the structures with isolated C atoms in three–fold sites are unfavoured at all coverages. Anyway, the minimum energy structures at 0.5 ML (Fig. 4 (a), (b) and (c)) are not fully compatible with our experimental results, because neither the number of non–equivalent core level components nor their relative spectral weights are correctly reproduced.

A value comparable with the experimental SCLS of the S_3 component (+570 meV) can be obtained only if the carbon coverage is increased from 0.5 to 0.75 ML. In particular, the models which correctly account for the experimental BE of the S_3 component are only the ones with C atoms adsorbed in adjacent sites in a trimer configuration (see Fig. 4 (f-g)). However, these structures are still quantitatively incompatible with our experimental data; the measured S_3 component, in fact, is too weak to fit any of the theoretical trimer models, and, most importantly, none of the simulated structures accounts for the observation of a single peak in the C 1s core level spectrum, which seemingly indicates the presence of a unique C species.

On the other hand, the structure with C atoms in interstitial subsurface sites (indicated by a hollow light blue circle in model(l)) yields a maximum core shift of only +476 meV for the first layer Re atoms that are coordinated with three C atoms on the plane and one in an interstitial site underneath. By contrast, the formation of hexagonal C rings proposed in models (e) and

(n) results in core level shifts above 700 meV, too large to fit the experimental data.

From the above discussion, we can reasonably conclude that the overlayer generating the observed $c(4\times2)$ pattern does not correspond to a single, well–ordered C phase. This is also supported by our LEEM results, showing that the Re surface is only partially covered by $c(4 \times 2)$ islands. We believe that the $c(4\times2)$ phase is mainly formed by C atom sitting in three–fold sites, as in model (d). However, also according to our DFT calculations, this is not the thermodynamically most stable configuration, so that the local formation of trimers must be considered in order to account for the experimentally observed SCL component at +570 meV. We can reasonably conclude that the absence of multiple components in the C 1s core level spectrum can be either ascribed to a low surface density of the minority population, or to our difficulty in detecting very small amounts of carbon.

We will see in the following that the local configuration with C trimers is typical of the carbide structure that forms at higher temperature.

3.2. High temperature carbon overlayers

In order to study the evolution of the C adlayers on Re(0001) and to investigate the possible formation of GR on this substrate, we explored temperature and pressure conditions that differ from the ones used to obtain the $c(4 \times 2)$ carbon phase.

As a first trial, we exposed the Re(0001) substrate to C_2H_4 at room temperature for a long period, up to a dose of more than 20 L (beyond the saturation limit), and subsequently annealed the sample to higher temperature. We repeated this procedure for several different annealing tem-

peratures between 850 and 1100 K, but the formation of an extended, ordered GR layer was never observed. This is different from what reported for Ru(0001), where the annealing of an amorphous carbon layer results in the formation of GR [38, 39]. Our results indicate that other methods, like the high–temperature annealing of surface carbides [2], or C monomer and dimer species [40], which have been successfully used to grow GR on other substrates, fail on Re (0001). Both our μ-LEED and photoemission data, instead, indicate that, upon annealing of the C_2H_4–presaturated Re(0001) surface, only local GR patches form on the surface. In fact, the moiré LEED pattern distinctive of GR, is visible only in few selected areas of the sample, while, in the other regions, LEED exhibits the (1×1) pattern of the clean surface. At the same time, the C 1s core level spectrum shows the double–peak structure characteristic of GR/Re(0001) -as will be explained in detail later on–, but the low intensity of the photoemission signal and the broad shape of the two peaks clearly indicate that the C layer covers only a limited area of the sample and is highly defective. We hence conclude that annealing of a well–ordered $c(4 \times 2)$ overlayer above 750 K leads to bulk dissolution, depleting the C coverage. This is a first indication that thermally activated C subsurface migration competes against the formation of stable surface C phases.

The second recipe we tested consisted of exposing the Re surface to a flux of C_2H_4 at high sample temperature, following a procedure which is routinely used on a number of substrates (e.g. Pt, Rh, Ir, Ru [2]). Several combinations of the experimental parameters (temperature, gas pressure, exposure time) were tried, but none of them led to the formation of a well-ordered GR layer.

At T>750 K, in fact, the thermal decomposition of C_2H_4 on Re(0001) results in a competitive interplay among three processes: GR growth, surface carbide formation, and C bulk dissolution.

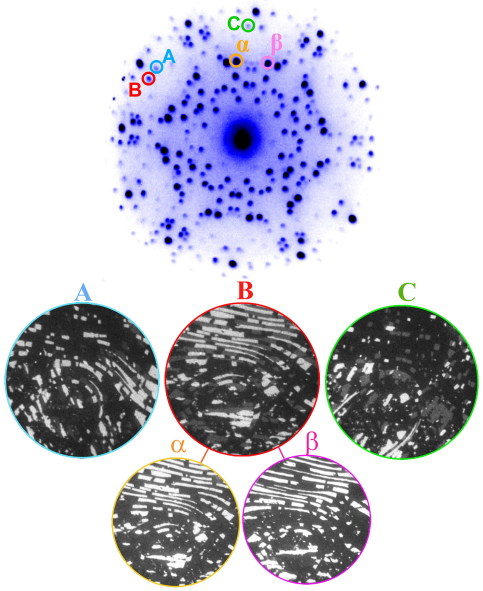

Figure 5: Top: LEED pattern of the surface carbide structure ($E = 40$ eV). Bottom: DF LEEM images ($E = 47$ eV, f.o.v.=4 µm) of three non–equivalent domains (A, B and C), related by an in–plane rotation of 120°. α and β indicate the two non–equivalent subdomains forming domain B, related by an in–plane rotation of ∼12°. The surface carbide was prepared by exposing the Re surface to a flux of C_2H_4 molecules (p= 2×10^{-7} mbar) and repeatedly annealing the sample up to 1200 K. This procedure allows allows a uniform carbide layer extending over the whole sample with no signs of GR formation.

Basically, we observed that a combination of high temperature and low C_2H_4 pressure (p<1×10^{-6} mbar, typically used on other substrates to obtain high quality GR layers, because of the lower density of ensuing nucleation centres) in our case favours C subsurface migration. On the other hand,

if the pressure is high enough (to ensure that the flux of impinging hydrocarbon molecules is larger than the rate of C bulk dissolution), GR can in principle grow on the surface. Unfortunately, though, the thermally activated formation and diffusion of defects induces a depletion of the C layer and the simultaneous formation of a new ordered phase, later identified as a surface carbide, as indicated by the appearance of a new, sharp LEED pattern (Fig. 5 (top)), whose complex geometry can be described, using the Park–Madden notation, by the following matrix:

$$\begin{pmatrix} \vec{b}_1 \\ \vec{b}_2 \end{pmatrix} = \begin{pmatrix} 7 & 0 \\ 2 & 5 \end{pmatrix} \begin{pmatrix} \vec{a}_1 \\ \vec{a}_2 \end{pmatrix} \tag{2}$$

where $\vec{b}_1, \vec{b}_2$ indicate the unit cell vectors of the overlayer, and $\vec{a}_1, \vec{a}_2$ are the primitive vectors of the Re(0001) lattice. Symmetry considerations led us to the conclusion that the observed pattern results from the superposition of three non–equivalent domains rotated by 120° from each other. This was confirmed by dark field LEEM experiments, which allowed us to isolate the regions of the sample contributing to non–equivalent diffraction spots (labelled A, B and C in Fig. 5). Inside each domain, we further distinguished two non–equivalent subdomains related by an in–plane rotation of ∼12° (labelled α and β in Fig. 5).

The LEED pattern of a single subdomain exhibits parallel arrays of evenly spaced spots, whose diffraction intensity is inversely proportional to the diffraction order (i.e. the lowest–order spots are the brightest), a behaviour typical of multiple scattering phenomena.

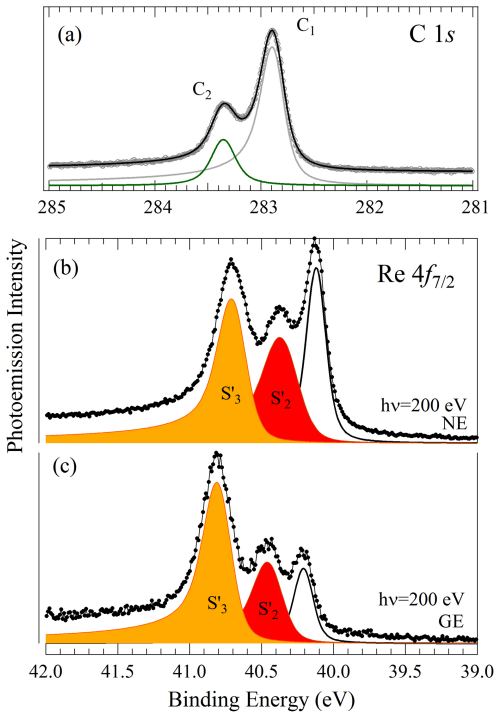

Figure 6: (a) C 1s spectrum of the Re surface carbide; (b-c) High resolution Re $4f_{7/2}$ core level spectra, acquired at $h\nu = 200$ eV, at (b) normal and (c) grazing emission.

Interestingly, also the $R(15 \times 3)$ carbide structure on W(110) shows a similar LEED pattern, where the superposition of rotational domains has occasionally been observed [41–45].

The C 1s core level spectrum of the Re surface carbide (Fig. 6 (a)) shows a distinctive double–peak structure, with two core level components (labelled C_1 and C_2), centred at 282.85 eV and 283.35 eV, respectively. The comparison of this C 1s core level spectrum with that of the analogous species on W(110) [45] confirms a certain similarity between the two. In both cases, in fact, two core level components can be resolved in the spectrum; furthermore, they are located at similar BEs, displaying a relative shift of approximately

450 meV.

According to our DFT calculations for the C 1s core level BEs for the trimer structure shown in Fig. 4 (see details of model (g) in the bottom panel), C_A and C_C–type carbon atoms have the same BE, while C_B–type atoms are found at 0.6 eV higher BE, in fair agreement with the experimental findings. The BE difference between $C_{A/C}$- and C_B–type atoms clearly arises from distinct local configurations, very likely characterized by a different charge transfer from the substrate to the adsorbates. In addition, the experimental intensity ratio between the two C 1s core level components is 0.57, very close to the theoretical ratio of 1 : 2 between the populations of C_B– and $C_{A/C}$–type atoms, which locally form the trimer structure (Fig. 4 bottom).

The Re $4f_{7/2}$ core level spectrum of this new phase (Fig. 6(b)-(c)) shows, as in the case of the $c(4\times2)$ phase, a suppression of the photoemission signal from uncoordinated surface atoms, while two new components (labelled S_2' and S_3') are seen to grow on the high BE side of the bulk peak. Most notably, these two components are located at BEs very similar to those of the S_2 and S_3 peaks in the $c(4\times2)$ structure.

The intensity ratio between S_2' and S_3' exhibits a strong dependence on the photoemission angle (compare Fig. 6(b) and (c)), with a strong relative increase of the S_3' component at grazing emission, which seems to indicate a predominant surface-like character of the latter.

The S_2' component also exhibits a similar, though less marked, increase with respect to the bulk component at grazing emission. We can therefore reasonably conclude that both S_2' and S_3' originate from top–layer substrate atoms found in similar local configurations (also in terms of C−Re bonding)

to those of surface Re atoms in the low temperature C phase.

Although our LEED analysis enabled us to determine the size and periodicity of the surface carbide unit cell, we cannot yet draw conclusions about the details of the atomic structure. Unfortunately, in fact, the size and complexity of the unit cell did not allow us to determine the minimum energy structure by means of DFT calculations. Our results, however, clearly indicate that the C trimer shown in the bottom panel of Fig. 4 (corresponding to cell (g)) generates the observed surface core level shifted component at +570 meV. We therefore believe that carbon trimers are the building blocks of the surface carbide phase.

Their presence, although in a limited amount, already accompanies the formation of the $c(4\times2)$ structure, in the form of layer defects. Their concentration subsequently increases and reaches a maximum when the diffraction spots of the pattern in Fig. 5 show the their highest intensity. In this new configuration, carbon forms clusters of 3 atoms adsorbed in adjacent sites in an hcp–fcc–hcp sequence, which produces a significant modification of the surface morphology. In particular, the C atom in the middle is found at 0.37 Å in–plane distance from the straight line defined by the two neighbouring atoms, and is 0.32 Å above the plane of the other atoms (see Fig. 4–bottom). We also notice an increase in the height of the first layer Re atoms placed just below the trimers, which have an average distance of 1.37 Å from the substrate. In addition, we observe that the trimer structure produces a visible zig–zag distortion of the Re atoms in the [1000] direction. We cannot exclude the occurrence of a surface reconstruction, as previously proposed for the $R(15\times3)$/W(110) structure [46].

In conclusion, it is clear that the appearance of the carbide phase over a wide temperature range, from 750 to 1100 K, poses a significant limitation to the growth of an extended GR layer.

3.3. High temperature GR formation

The results reported above justify the conclusion that, to grow GR on Re, a route alternative to those typically adopted on other transition metal surfaces must be used. In the search for an effective growth method, the following factors, affecting the quality of the resulting GR layer, should be considered. First of all, the temperature should be high enough to enhance the rate of C−C bond formation, but not so large to favour the breakup of the C layer. The hydrocarbon pressure, on the other hand, should be high enough to enable the initial C cluster nucleation, but not too high, otherwise the simultaneous formation of multiple nucleation centres would eventually result in a defective C layer, with a high density of domain boundaries.

The recipe we ultimately worked out consists of preliminarily saturating the Re substrate with C_2H_4 at room temperature, and subsequently performing a series of rapid heating–cooling cycles between 300 and 1100 K in C_2H_4 atmosphere ($p_{C_2H_4} = 5 \times 10^{-7}$ mbar). This procedure yields a high quality GR layer, as judged from the sharp LEED pattern (see Fig. 7 (d)), which exhibits the typical periodicity of a moiré coincidence lattice when GR is grown on many TMs [47], and by the low diffuse background.

We believe the success of this growth method can be explained by the following two arguments: (i) heating the sample in cycles rather than keeping it at high temperature for a prolonged period reduces the probability of C−C bond breaking and prevents possible damages to the C layer; (ii) as will be

explained in detail in the following, a single CVD annealing cycle is not sufficient to cover the whole sample with graphene.

In order to tackle the dynamics of the GR formation process, and to study the effect of the temperature on the overlayer, we performed an *in situ* LEED experiment, in which we monitored the evolution of the diffraction pattern while preparing GR by a series of annealing cycles in ethylene atmosphere. A waterfall plot showing the evolution of the LEED pattern along the radial direction between the $(\bar{1}, 0)$ and the $(1, 0)$ spots of the substrate is reported in Fig. 7 (a). From the plot in Fig. 7 (c), it is clear how the diffraction spots associated with the moirè periodicity increase in intensity at each annealing cycle [3], meaning that the GR lattice is growing in an ordered way and extending over the metal substrate. The intensity losses in correspondence of the temperature maxima, which produce the oscillating behaviour of the curve, are simply due to the Debye–Waller thermal attenuation effect.

Another interesting phenomenon accompanying GR formation is the modification of the moiré lattice constant: the reciprocal lattice spacing between the (0.92,0) moiré diffraction spot and the (0,0) spot of the substrate, in fact, increases between consecutive annealing cycles. The maximum relative variation amounts to about 3%. This indicates that the GR lattice undergoes a partial structural rearrangement and that the moiré supercell slightly contracts as the carbon layer extends over the substrate. Notably, a similar effect has been reported by Blanc *et al.* [48] for GR on Ir(111). In particular, the authors observed large lattice strain effects, above 2%, during GR growth

[3] Only the (0.92,0) moirè diffraction spot is shown in the Figure

by CVD on Ir(111), which were attributed to the presence and diffusion of vacancies formed during CVD. More specifically, they propose that the progressive filling of vacancies during CVD and the thermally activated diffusion of small vacancies to the edges of GR islands, where they disappear, reduce the tensile strains, leading to a decrease of the moiré lattice parameter at increasing C coverage. It is reasonable to assume that a similar mechanism can explain the analogous effect observed for GR/Re(0001).

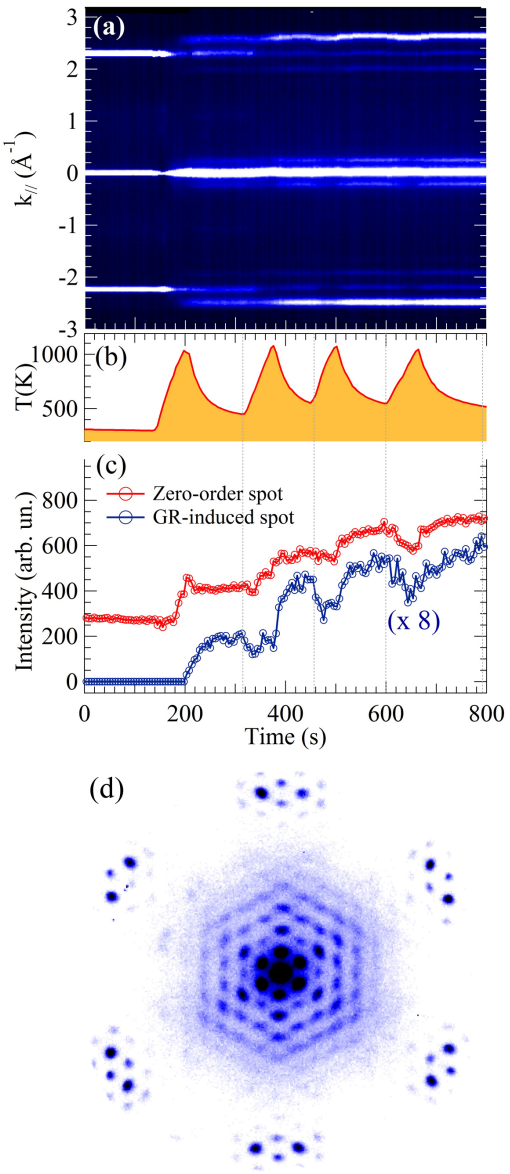

Figure 7: (a) LEED line profile evolution of GR/Re(0001), recorded *in situ* during C_2H_4 CVD on Re(0001) through a series of heating/cooling cycles. (b) Sample temperature *vs* time during C_2H_4 CVD. (c) Intensity evolution of the (0,0) (red) and of the (0.92,0) moirè (blue) LEED spot during GR formation on Re(0001). (d) Moirè LEED pattern of a high quality GR layer on Re(0001).

The moiré superlattice periodicity was estimated from a line profile analysis of the LEED patterns of GR/Re(0001) acquired at various electron energies, revealing that the moiré cell is formed by (10×10) unit cells of GR over (9×9) unit cells of the substrate. It should be recalled that the lattice parameter of pristine GR is 2.46 Å, while that of Re(0001) is 2.71 Å. Since each GR unit cell contains two C atoms, the total C coverage yielded by a single C layer extending over the entire substrate is $2 \times (10 \times 10)/(9 \times 9) = 2.47$ ML, corresponding to a density of 3.74×10^{15} C atoms cm^{-2}.

On the basis of the structural information obtained in this preliminary stage, we performed detailed DFT calculations. Our simulations [49] indicate that the moiré cell is significantly corrugated, with a C−Re distance between 2.14 and 3.87 Å (relative to the top layer of the substrate) and nearly 75% of the C atoms within 3 Å from the metal substrate. More specifically, the internal regions of the moiré cell, where the C atoms are found either in fcc or in on–top position, are on average characterized by a shorter C−Re distance, while, at the corners of the moiré cell, the C layer is slightly lifted relative to the substrate.

The DFT–calculated positions of the 200 C atoms in the moiré cell were analysed to determine the C−C bond length distribution, calculated as the average distance of each C atom from the three nearest neighbouring atoms. It turns out that the C−C bond length inside the moiré cell ranges between 1.43 and 1.47 Å, with a relative variation of 3% and an average value of 1.45 Å. These data should be compared with the C−C bond length of pristine GR, which is 1.42 Å. Specifically, a significant C−C bond stretching is observed in the buckled regions of the moiré cell, where the C layer is closer to the

substrate, while, at the corners and along the borders of the cell, the average C−C distance is comparable to that of free-standing GR. In addition, a clear dependence between the C−C bond length and the C−Re distance is found, as can be seen in Fig. 8(a-b).

Interestingly, we observe that the atoms inside the 'valleys' of the moiré cell (see inset of Fig. 8 (a)) are not equivalent as far as the C−C bond distance is concerned. Namely, the stretching is smaller for B–type C atoms (the ones in on–top sites, which display an average C−C bond length of 1.45 Å), and larger for A–type atoms, which are not directly bonded to a first–layer Re atom, and for which the C−C bond length is on average nearly 1% (0.01 Å) larger than for the others. After the structural characterisation of the system, a fundamental insight into the electronic properties of GR/Re(0001) was achieved through the analysis of the C 1s core level photoemission spectrum: the spectral profile, in fact, is strongly affected by the coupling between GR and the substrate.

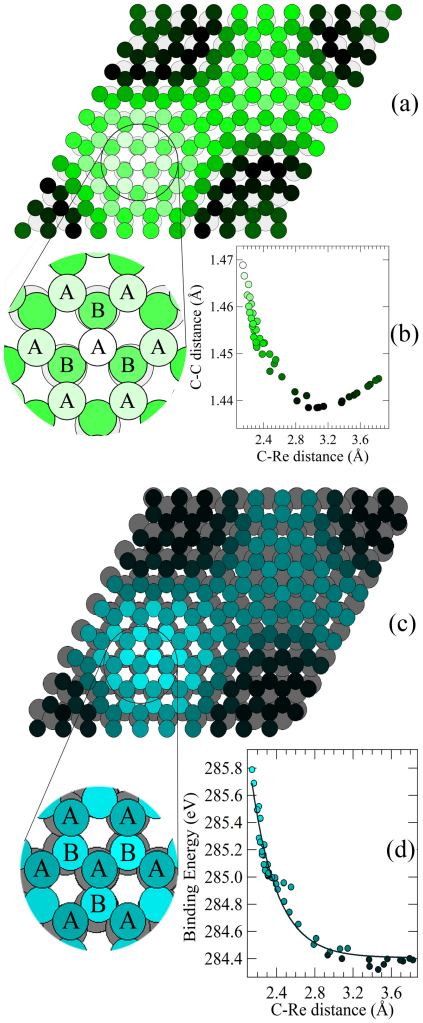

Figure 8: (a) DFT–calculated C−C nearest neighbour distance inside the moiré cell of GR/Re(0001). (b) Plot of the calculated C−C nearest neighbour distance *vs* C−Re distance. The colour scale in both (a) and (b) is proportional to the C−C bond length. (c) DFT–simulated moiré cell of GR/Re(0001) (only the first layer of the substrate is shown). (d) Calculated C 1*s* core level BEs *vs* C−Re distance, showing a monotonic dependence between the two quantities. The blue color scale reflects the atomic core level BEs.

The high-energy resolution C 1*s* core level spectrum of GR/Re(0001) (see

Supplementary Data) exhibits two main components, separated by 700 ± 20 meV, which suggests a strong interaction between the C layer and the substrate, based on the analogy with GR/Ru(0001) and Rh(111) [49]. Following the interpretation proposed for the latter systems, we assigned the low BE component (W) to the weakly interacting regions of the GR layer and the peak at higher BE (S) to the strongly interacting ones.

The large Lorentzian width of the high BE component [4] resembles what found for similar systems, suggesting the presence of a manifold of unresolved spectral features. For GR/Re(0001), the inadequacy of the two–peak model, which makes a net distinction between 'weakly' and 'strongly' interacting regions of the C layer, has recently been addressed by DFT [49]. In that work, we calculated the C 1s core level BE of each of the 200 C atoms in the moiré cell, including both initial and final state effects. Our results indicated a continuous distribution of the core level BEs in the range $284.3 \div 285.8$ eV, and evidenced a clear correlation between the latter and the C−Re distance: a smaller C–substrate distance, in fact, is reflected in a higher BE. The simulated spectral distribution was then fitted to a sum of 200 Doniach-Šunjič (DS) functions convoluted with a Gaussian profile. The BE of each component was fixed to its DFT–calculated value. The excellent agreement between experimental and simulated data proved that the double–peak shape of the C 1s spectrum actually arises from a quasi–continuous, rather than binary distribution of the C−Re distances in the nanomesh [49].

A further improvement in the quality of the fit was achieved by intro-

[4] please refer to the table of the line shape parameters in the Supplementary Data

ducing an exponential dependence of the type $A\exp(-Bd)$ (with A and B free fitting parameters) between the Lorentzian FWHM of the peaks and the C−Re distance. This assumption relies on the consideration that a larger or smaller distance between the C atoms and the substrate affects the local electronic structure, and hence the core–hole relaxation probability, in the region considered. The values of the A and B parameters obtained from our fit ($A = 1.015 \pm 0.100$ eV; $B = 0.536 \pm 0.05$ Å^{-1}), indicate, as expected, a reduction of the average core–hole lifetime for the low–lying, strongly interacting C atoms of the moiré cell. The values we correspondingly obtain for the Lorentzian widths are in the range $130 \div 320$ meV. The lower limit of 130 meV compares fairly well with the experimentally found Lorentzian widths of GR/Ir(111), reported in previous studies [50, 51].

As already pointed out in our previous work [49], some distinctive common trends can be identified for both the C 1s core level BE distribution inside the moiré cell and the corresponding distribution of the C−Re distances. According to our DFT calculations, the low–lying regions of the C layer are characterized by a stronger C-metal interaction, while the C atoms at the edges, which are found at a larger distance from the substrate, are more weakly interacting.

An analogous relationship is found also between the C 1s core level BE distribution and the C−C bond length distribution. Specifically, we observe that the C atoms in the strongly buckled *fcc* and *hcp* regions of the moiré cell have a higher C 1s core level BE, while the atoms in the *atop* regions are characterized by a smaller BE.

A closer inspection of the C 1s core level BE distribution inside the 'val-

leys' of the moiré cell (see inset of Fig. 8 (c)) reveals a similar trend to the one found for the C−C bond distance distribution. In this case, in fact, the C atoms in on–top sites, labelled A, are characterized by a BE nearly 500 meV smaller than B–type atoms.

In conclusion, inside the buckled regions of the moiré cell, the C atoms on top of a first layer Re atom exhibit a smaller C 1s core level BE and a slight C−C bond length contraction. This behaviour is consistent with our previous observations on the thermal evolution of the C 1s core level spectrum of GR/Ir(111) [52]: the annealing–induced C−C bond length stretching, in fact, results in an overall shift of the C 1s core level spectrum to higher BEs.

3.4. Competition between C phases and thermal stability of GR

In the high temperature range we observe an intriguing interplay among three competing processes: GR growth, surface carburisation and carbon bulk dissolution. The prevalence of one process over the others depends on two key factors: the temperature of the sample and the background hydrocarbon pressure.

All our experimental observations, however, indicate that GR/Re(0001) is not stable at T$\geq$1000 K. Above this temperature, in fact, both GR annealing at increasing temperature and its prolonged annealing at constant temperature result in the irreversible depletion of the C layer and in the simultaneous appearance of surface carbides. With reference to Fig. 9, which reports the C 1s photoemission spectra measured while annealing the GR/Re(0001) system, we observe that, although the most evident changes occur above 1200 K, some significant modifications take place already between 1000 and 1200 K: although the double-peak structure of GR is preserved, in fact, the strongly

interacting C 1s core level component (S) significantly loses intensity upon annealing [49]. For temperatures between 1100 and 1200 K, the overall intensity of the C 1s photoemission signal rapidly decreases, and, at the same time, the photoemission signal associated with surface carbides gains intensity.

To shed light on these phenomena, we carried out distinct sets of experiments, in which we focused on the evolution of the C layer, either as a function of the temperature, or as a function of the time -with the sample kept at fixed temperature.

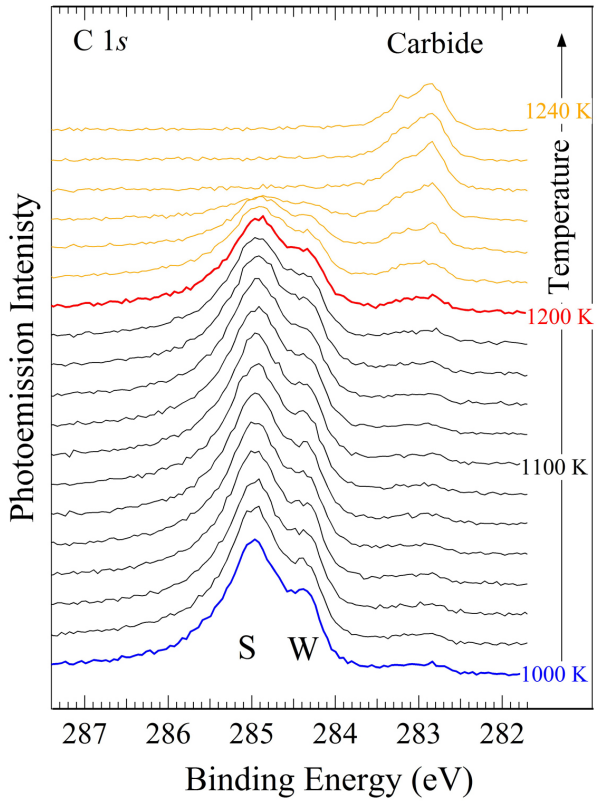

Figure 9: Photoemission intensity evolution of the different C 1s spectral components during annealing of GR/Re(0001) from 1100 to 1240 K.

In the constant–temperature XPS experiments [53], we monitored the evolution of the C 1s core level spectrum of the the GR–covered substrate while annealing it at a constant heating rate. The initial stage of the annealing above 1000 K is characterised by an evident intensity loss of the double peak structure typical of GR, followed by the appearance, at lower BE, of the two–peak structure characteristic of surface carbides. Above a certain temperature ($\geq$1350 K), however, also these spectral features lose intensity and eventually disappear, which clearly indicates the complete bulk dissolution of the C initially present on the surface.

The same experiment was repeated also in LEED and LEEM mode. Annealing of a well–ordered GR–covered surface first results in the intensity attenuation of the moiré diffraction pattern, and subsequently in the appearance of the complex diffraction pattern characteristic of the carbidic phase. The transition from GR to carbide is quite abrupt: within a temperature range of 100 K the process is mostly completed. Interestingly, although the diffraction spots of the moiré superlattice lose intensity upon annealing, thus indicating a depletion of the C layer caused by bulk dissolution, they keep a sharp and narrow shape over the whole T range before vanishing, as reflected in their Lorentzian width, which is basically unchanged. This means that the long range order of the C layer is substantially preserved upon annealing, hence proving that the disruption of the GR layer does not proceed by reaction fronts, but rather involves the random formation of point lattice defects.

Consistently with the XPS results, the LEED data confirm that the surface carbide species is gradually bulk–dissolved upon annealing: above

1350 K, in fact, also the diffraction pattern of surface carbides fades away until only the (1×1) pattern of the clean surface remains visible.

To gain complementary information on the evolution of the C layer in real space, the same experiment was repeated also in microscopy mode. The LEEM image of GR–covered Re(0001) at the start of the experiment exhibits a uniform grey shade, as visible in Fig. 10(a). The onset of carbide nucleation is characterized by the appearance of dark spots on the surface, both at the steps and on the terraces (Fig. 10(b)), which progressively expand to cover great part of the surface (Fig. 10(c)-(d)). Upon further annealing, the area of the carburized surface (Fig. 10(g)) shrinks upon C bulk dissolution, so that in the end only the bare Rhenium surface remains visible (Fig. 10(h)).

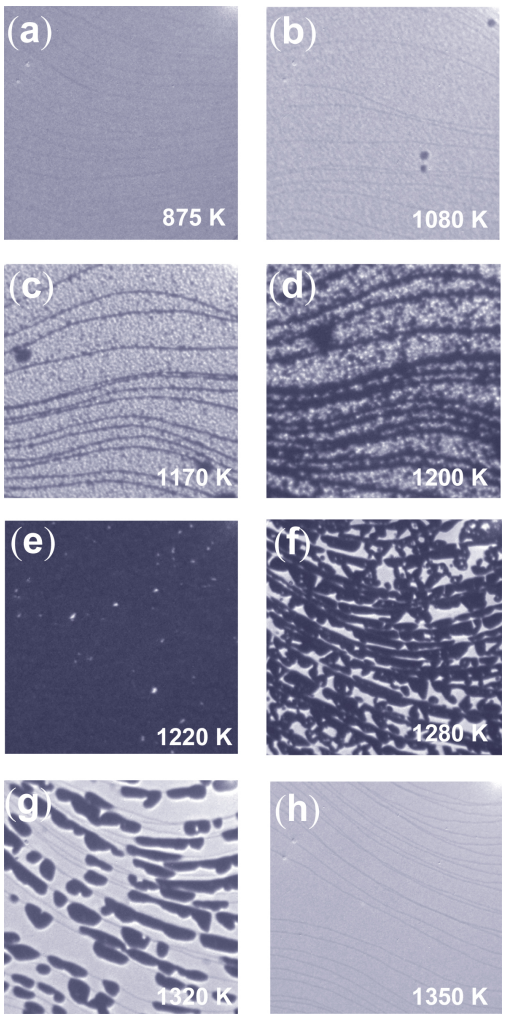

Figure 10: BF LEEM images (E=4 eV, f.o.v.: 4 µm) acquired during the annealing of GR/Re(0001) at increasing temperature (see insets in the figures). (a) GR-covered Re surface at the beginning of the experiment, showing a uniform grey shade; (b) carbide nucleation, accompanied by the appearance of dark spots at the steps and on the terraces; (c-e) expansion of the surface carbide phase; (f-g) thermally-induced bulk dissolution of the surface carbides (the bright halo around the dark spots is caused by the different work function of the clean and carburised regions of the substrate); (h) bare Re(0001) surface visible after C bulk dissolution.

It is worth reporting that the same behaviour, namely the transition GR→carbides→bulk dissolution is observed also when the sample is annealed in an ethylene background, although with slightly different temperature parameters. More specifically, an increased hydrocarbon pressure pushes the transition temperatures to higher values.

It is instructive to compare the high temperature thermal behaviour of GR/Re(0001) with that of GR/Rh(111) [54]. First and foremost, GR growth on both substrates requires an accurate selection of the experimental growth conditions, in particular of the annealing rate during hydrocarbon CVD. Moreover, both systems are characterised by a complex interplay between GR and carbides, but there are some relevant differences. First, GR/Rh(111) is stable over a considerably larger temperature range (808-1053 K) than GR/Re(0001). In addition, differently from what observed in the case of GR/Re(0001), carbides on Rh are energetically less stable than GR, which precludes the conversion of GR into carbides, but makes the reverse process possible. In fact, when carbides and GR coexist on the Rh(111) surface, the carbides eventually transform into GR islands, which progressively grow in size over time.

Another system which is in many respects similar to Re(0001) is Fe(110). Also this substrate, in fact, interacts strongly with carbon, so that GR growth is limited to a very narrow window of the experimental parameter space [55]. Differently from Re, however, Fe is characterised by a higher carbon bulk solubility and tends to form a stable bulk carbide phase, Fe_3C. It is therefore clear that the possibility to grow GR on strongly interacting metals is ultimately determined by the accurate choice of the experimental growth

parameters (temperature, hydrocarbon pressure, annealing procedure), and does not depend on the nature of the possible C phases competing with GR on a specific substrate.

Besides the experiments at increasing temperature, we monitored also the thermal evolution of GR when the sample is kept at constant temperature (in the range 1100–1200 K). As previously reported [49], the GR layer does not resist at high temperature, and the process of C−C bond breaking, which has an estimated activation barrier of 3.5 ± 0.7 eV, is favoured in the strongly buckled regions of the moiré cell, where it takes place through the diffusion of C monolayer vacancies.

It is important to stress here that the process of GR layer breaking observed in our case is markedly different from what reported by Gall *et al.* [56], who state that the breakup of C−C bonds occurs at the edges of GR islands.

4. Conclusions

In conclusion, our experimental and theoretical results demonstrate that the growth of high–quality GR films is possible also on Re(0001), although it is restricted to a small region of the experimental parameter space (substrate temperature, hydrocarbon gas pressure and exposure time). More specifically, while the low temperature regime is dominated by the formation of a chemisorbed carbon phase with $c(4 \times 2)$ periodicity, at high temperature we observe a complex interplay between two competing species, GR and surface carbides, whose formation is in turn opposed by carbon bulk dissolution. By carefully exploring the parameter space, it is still possible to grow a single layer of GR, free from surface carbides and avoiding carbon bulk saturation

of the Re(0001) crystal, at temperatures which are significantly lower than previously reported [21].

In this way, despite the competition with a rival species, the quality of the so–obtained GR layer, as judged from our diffraction and microscopy data, is very high. At high temperature, the disruption of GR is a very intriguing phenomenon, which proceeds through the partial conversion of GR into surface carbides, and eventually leads to carbon migration to the subsurface region of the sample.

Our findings are promising, because they suggest that, under appropriate conditions, also other substrates, like W and Ti, which are well known to interact strongly with C and to form carbides, might be good candidates for the supported growth of GR. Most importantly, we believe our method can be effective at temperatures below the carbon bulk solubility, thanks to the favourable interplay between kinetics and thermodynamics under these conditions.

Acknowledgments

This work was supported by the Università degli Studi di Trieste through the program *Finanziamento per Ricercatori di Ateneo*, and by the the MIUR under the program PRIN2010 for the project entitled 'GRAF. Frontiers in GR Research: understanding and controlling Advanced Functionalities'. D.A. and A.B. acknowledge the Royal Society for support. Calculations were run on the HECToR national facility in the U.K..

References

1. Li, Z., Wu, P., Wang, C., Fan, X., Zhang, W., Zhai, X., et al. Low-temperature growth of graphene by chemical vapor deposition using solid and liquid carbon sources. *ACS Nano* 2011;**5**(4):3385–3390. doi:10.1021/nn200854p.

2. Batzill, M.. The surface science of graphene: Metal interfaces, cvd synthesis, nanoribbons, chemical modifications, and defects. *Surf Sci Rep* 2012;**67**(34):83 – 115. doi:10.1016/j.surfrep.2011.12.001.

3. Ren, W.C., Gao, L.B., Ma, L.P., Cheng, H.M.. Preparation of graphene by chemical vapor deposition. *Carbon* 2011;**49**(8):2881. doi:http://dx.doi.org/10.1016/j.carbon.2011.02.043.

4. Soldano, C., Mahmood, A., Dujardin, E.. Production, properties and potential of graphene. *Carbon* 2010;**48**(8):2127 – 2150. doi:http://dx.doi.org/10.1016/j.carbon.2010.01.058.

5. Li, X., Cai, W., An, J., Kim, S., Nah, J., Yang, D., et al. Large-area synthesis of high-quality and uniform graphene films on copper foils. *Science* 2009;**324**(5932):1312–1314. doi:10.1126/science.1171245.

6. Bae, S., Kim, H., Lee, Y., Xu, X., Park, J.S., Zheng, Y., et al. Roll-to-roll production of 30-inch graphene films for transparent electrodes. *Nature* 1995;**376**:238–240. doi:10.1038/376238a0.

7. Tontegode, A.. Carbon on transition metal surfaces. *Prog Surf Sci* 1991;**38**:201–429. doi:10.1016/0079-6816(91)90002-L.

8. Shelton, J., Patil, H., Blakely, J.. Equilibrium segregation of carbon to a nickel (111) surface: A surface phase transition. *Surf Sci* 1974;**43**:493 – 520. doi:http://dx.doi.org/10.1016/0039-6028(74)90272-6.

9. Wintterlin, J., Bocquet, M.L.. Graphene on metal surfaces. *Surf Sci* 2009;**603**(1012):1841 – 1852. doi:http://dx.doi.org/10.1016/j.susc.2008.08.037.

10. Coraux, J., N'Diaye, A., Busse, C., Michely, T.. Structural coherency of graphene on Ir(111). *Nano Letters* 2008;**8**:565. doi:10.1021/nl0728874.

11. N'Diaye, A., Coraux, J., Plasa, T., Busse, C., Michely, T.. Structure of epitaxial graphene on Ir(111). *New J Phys* 2008;**10**:043033. doi:10.1088/1367-2630/10/4/043033.

12. Coraux, J., N'Diaye, A., Engler, M., Busse, C., Wall, D., Buckanie, N., et al. Growth of graphene on Ir(111). *New Journal of Physics* 2009;**11**:023006. doi:10.1088/1367-2630/11/2/023006.

13. Sutter, P., Sadowski, J.T., Sutter, E.. Graphene on Pt(111): Growth and substrate interaction. *Phys Rev B* 2009;**80**:245411. doi:10.1103/PhysRevB.80.245411.

14. Levy, N., Burke, S.A., Meaker, K.L., Panlasigui, M., Zettl, A., Guinea, F., et al. Strain-induced pseudomagnetic fields greater than 300 tesla in graphene nanobubbles. *Science* 2010;**329**(5991):544–547. doi:10.1126/science.1191700.

15. Gao, M., Pan, Y., Huang, L., Hu, H., Zhang, L.Z., Guo, H.M., et al. Epitaxial growth and structural property of graphene on Pt(111). *Applied Physics Letters* 2011;**98**(3):033101. doi:http://dx.doi.org/10.1063/1.3543624.

16. Fujita, T., Kobayashi, W., Oshima, C.. Novel structures of carbon layers on a Pt(111) surface. *Surface and Interface Analysis* 2005; **37**(2):120–123. doi:10.1002/sia.1945.

17. Gao, J.H., Sagisaka, K., Kitahara, M., Xu, M.S., Miyamoto, S., Fujita, D.. Graphene growth on a Pt(111) substrate by surface segregation and precipitation. *Nanotechnology* 2012;**23**(5):055704. doi:http://stacks.iop.org/0957-4484/23/i=5/a=055704.

18. Liu, N., Fu, L., Dai, B., Yan, K., Liu, X., Zhao, R., et al. Universal segregation growth approach to wafer-size graphene from non-noble metals. *Nano Letters* 2011;**11**(1):297–303. doi:10.1021/nl103962a.

19. Fujita, D., Yoshihara, K.. Surface precipitation process of epitaxially grown graphite (0001) layers on carbon-doped nickel(111) surface. *Journal of Vacuum Science & Technology A* 1994;**12**(4):2134–2139. doi:10.1116/1.579150.

20. Fujita, D., Schleberger, M., Tougaard, S.. Xps study of the surface enrichment process of carbon on C-doped Ni(111) using inelastic background analysis. *Surf Sci* 1995;**331333**(0):343 – 348. doi:10.1016/0039-6028(95)00312-6.

21. Gall, N., Rut'kov, E., Tontegode, A.. Two dimensional graphite films on metals and their intercalation. *Int J Mod Phys B* 1997;**11**:1865–1911. doi:10.1142/S0217979297000976.

22. Baraldi, A., Comelli, G., Lizzit, S., Kiskinova, M., Paolucci, G.. Real-time x-ray photoelectron spectroscopy of surface reactions. *Surf Sci Rep* 2003;**49**(6-8):169 – 224. doi:10.1016/S0167-5729(03)00013-X.

23. Bauer, E.. Low energy electron microscopy. *Reports on Progress in Physics* 1994;**57**:895. doi:10.1088/0034-4885/57/9/002.

24. Locatelli, A., Aballe, L., Mentes, T.O., Kiskinova, M., Bauer, E.. Photoemission electron microscopy with chemical sensitivity: Speleem methods and applications. *Surface and Interface Analysis* 2006;**38**(12-13):1554–1557. doi:10.1002/sia.2424.

25. Altman, M.. Trends in low energy electron microscopy. *J Phys: Cond Matt* 2010;**22**:084017. doi:10.1088/0953-8984/22/8/084017.

26. Bauer, E.. Leem basics. *Surf Rev Lett* 1998;**5**:1275. doi:10.1142/S0218625X98001614.

27. Doniach, S., Šunjić, M.. Many-electron singularity in x-ray photoemission and x-ray line spectra from metals. *J Phys C: Solid State Phys* 1970;**3**(2):285. doi:10.1088/0022-3719/3/2/010.

28. Hohenberg, P., Kohn, W.. Inhomogeneous electron gas. *Phys Rev* 1964;**136**:B864–B871. doi:10.1103/PhysRev.136.B864.

29. Kohn, W., Sham, L.J.. Self-consistent equations including exchange and correlation effects. *Phys Rev* 1965;**140**:A1133–A1138. doi:10.1103/PhysRev.140.A1133.

30. Perdew, J.P., Burke, K., Ernzerhof, M.. Generalized gradient approximation made simple. *Phys Rev Lett* 1996;**77**:3865–3868. doi:10.1103/PhysRevLett.77.3865.

31. Blöchl, P.E.. Projector augmented-wave method. *Phys Rev B* 1994; **50**:17953–17979. doi:10.1103/PhysRevB.50.17953.

32. Kresse, G., Furthmüller, J.. Efficient iterative schemes for *ab initio* total-energy calculations using a plane-wave basis set. *Phys Rev B* 1996; **54**:11169–11186. doi:10.1103/PhysRevB.54.11169.

33. Kresse, G., Joubert, D.. From ultrasoft pseudopotentials to the projector augmented-wave method. *Phys Rev B* 1999;**59**:1758–1775. doi:10.1103/PhysRevB.59.1758.

34. Köhler, L., Kresse, G.. Density functional study of CO on Rh(111). *Phys Rev B* 2004;**70**:165405 (1–9). doi:10.1103/PhysRevB.70.165405.

35. Ducros, R., Housley, M., Alnot, M., Cassuto, A.. Ethylene and acetylene adsorption on Rhenium polycrystalline and Re(0001) surfaces. *Surf Sci* 1978;**71**(2):433–446. doi:10.1016/0039-6028(78)90343-6.

36. Miniussi, E., Hernández, E.R., Pozzo, M., Baraldi, A., Vesselli, E., Comelli, G., et al. Non-local effects on oxygen-induced surface core level shifts of Re(0001). *J Phys Chem C* 2012;**116**(44):23297–23307. doi:10.1021/jp304838g.

37. Saadi, S., Abild-Pedersen, F., Helveg, S., Sehested, J., Hinnemann, B., Appel, C.C., et al. On the role of metal step-edges in graphene growth. *J Phys Chem C* 2010;**114**(25):11221–11227. doi:10.1021/jp1033596.

38. Günther, S., Dänhardt, S., Ehrensperger, M., Zeller, P., Schmitt, S., Wintterlin, J.. High-temperature scanning tunneling microscopy study of the ordering transition of an amorphous carbon layer into graphene on Ruthenium(0001). *ACS Nano* 2013;**7**(1):154–164. doi:10.1021/nn303468j.

39. Lahiri, J., Miller, T., Adamska, L., Oleynik, I.I., Batzill, M.. Graphene growth on Ni(111) by transformation of a surface carbide. *Nano Letters* 2011;**11**(2):518–522. doi:10.1021/nl103383b.

40. Yuan, Q., Gao, J., Shu, H., Zhao, J., Chen, X., Ding, F.. Magic carbon clusters in the chemical vapor deposition growth of graphene. *J Am Chem Soc* 2012;**134**(6):2970–2975. doi:10.1021/ja2050875.

41. Stern, R.. Tungsten (110) surface characteristics in low–energy electron diffraction. *Appl Phys Lett* 1964;**5**:218–220. doi:10.1063/1.1723595.

42. Ollis, D., Boudart, M.. Surface and bulk carburization of tungsten single crystals. *Surf Sci* 1970;**23**:320–346. doi:10.1016/0039-6028(70)90156-1.

43. Bode, M., Pascal, R., Wiesendanger, R.. STM study of carbon–induced reconstructions on W(110): strong evidence for a surface lattice

deformation. *Surf Sci* 1995;**344**:185–191. doi:10.1016/0039-6028(95)00873-X.

44. Weinberg, W.H., Merrill, R.P.. Atomic and molecular diffraction and scattering from a tungsten carbide surface characterized by LEED. *J Chem Phys* 1972;**56**(6):2893. doi:10.1063/1.1677623.

45. Varykhalov, A., Rader, O., Gudat, W.. Structure and quantum–size effects in a surface carbide: W(110)/C−R(15 × 3). *Phys Rev B* 2005; **72**:115440–115449. doi:10.1103/PhysRevB.72.115440.

46. K.J. Rawlings, S.F., Hopkins, B.. A model for carburised W(100) and W(110). *J Phys C: Solid State Phys* 1981;**14**:5411. doi:10.1088/0022-3719/14/34/018.

47. Merino, P., Švec, M., Pinardi, A.L., Otero, G., Martín-Gago, J.A.. Strain-driven moiré superstructures of epitaxial graphene on transition metal surfaces. *ACS Nano* 2011;**5**(7):5627–5634. doi:10.1021/nn201200j.

48. Blanc, N., Jean, F., Krasheninnikov, A.V., Renaud, G., Coraux, J.. Strains induced by point defects in graphene on a metal. *Phys Rev Lett* 2013;**111**:085501. doi:10.1103/PhysRevLett.111.085501.

49. Miniussi, E., Pozzo, M., Baraldi, A., Vesselli, E., Zhan, R.R., Comelli, G., et al. Thermal stability of corrugated epitaxial graphene grown on Re(0001). *Phys Rev Lett* 2011;**106**:216101 (1–4). doi:10.1103/PhysRevLett.106.216101.

50. Lizzit, S., Zampieri, G., Petaccia, L., Larciprete, R., Lacovig, P., Rienks, E.D.L., et al. Band dispersion in the deep 1s core level of graphene. *Nature* 2010;**6**:345–349. doi:10.1038/376238a0.

51. Knudsen, J., Feibelman, P.J., Gerber, T., Grånäs, E., Schulte, K., Stratmann, P., et al. Clusters binding to the graphene moiré on Ir(111): X-ray photoemission compared to density functional calculations. *Phys Rev B* 2012;**85**:035407 (1–6). doi:10.1103/PhysRevB.85.035407.

52. Pozzo, M., Alfè, D., Lacovig, P., Hofmann, P., Lizzit, S., Baraldi, A.. Thermal expansion of supported and freestanding graphene: Lattice constant versus interatomic distance. *Phys Rev Lett* 2011;**106**:135501 (1–4). doi:10.1103/PhysRevLett.106.135501.

53. Baraldi, A., Comelli, G., Lizzit, S., Cocco, D., Paolucci, G., Rosei, R.. Temperature programmed x-ray photoelectron spectroscopy: a new technique for the study of surface kinetics. *Surf Sci* 1996;**367**(3):L67 – L72. doi:10.1016/S0039-6028(96)01126-0.

54. Dong, G., van Baarle, D., Rost, M., Frenken, J.. Graphene formation on metal surfaces investigated by in-situ scanning tunneling microscopy. *New Journal of Physics* 2012;**14**(5):053033. doi:10.1088/1367-2630/14/5/053033.

55. Vinogradov, N.A., Zakharov, A.A., Kocevski, V., Rusz, J., Simonov, K.A., Eriksson, O., et al. Formation and structure of graphene waves on Fe(110). *Phys Rev Lett* 2012;**109**:026101. doi:10.1103/PhysRevLett.109.026101.

56. Gall', N., Lavrovskaya, N., Rut'kov, E., Tontegode, A.. Thermal destruction of two-dimensional graphite islands on refractory metals (Ir, Re, Ni, and Pt). *Technical Physics* 2004;**49**(2):245–249. doi:10.1134/1.1648963.

List of captions for Figures and Tables

Figure 1 Thermal Desorption spectra of H_2 ($m/e = 2$) for different values of the ethylene exposure at T=170 K. Heating rate =2 K s^{-1}. In the insets are reported the disordered (1×1) LEED pattern of the Re(0001) surface after C_2H_4 adsorption at room temperature and (on the right) the experimentally determined H uptake curve.

Figure 2 (a) LEED pattern of the $c(4 \times 2)$ structure ($E = 55$ eV), in which three diffraction spots due to non–equivalent surface domains are differently highlighted. (b) Corresponding bright field image of the surface ($E = 4$ eV, field of view (f.o.v.): 2 µm). (c)–(e) Dark field LEEM images ($E = 16$ eV, f.o.v.: 2 µm) of the three non–equivalent domains corresponding to the LEED spots highlighted in (a).

Figure 3 (a) High resolution Re $4f_{7/2}$ core level spectra of clean Re(0001), acquired at normal emission with $h\nu = 200$ eV; the deconvolution into bulk (S_b) and surface (S_0) components is shown superimposed. (b, c) High resolution Re $4f_{7/2}$ core level spectrum of the $c(4 \times 2)$ structure, collected with $h\nu = 200$ eV, at normal (b) and grazing (c) emission.

Figure 4 Simulated structural models of C overlayers with coverages between 0.5 and 1.5 ML, assuming C adsorption in different surface sites.

The cells with $c(4 \times 2)$ symmetry are highlighted with a blue mark on the corresponding label; the other structures have (4×2) symmetry. Structure (l) also has a C atom in a subsurface interstitial site, which is indicated by a light blue circle. . For each structure, the C coverage and the total energy are indicated on the left. The values of the calculated SCLSs (in meV) are shown, superimposed to each first-layer Re atom in the different cells. Details of model (g) are highlighted in the bottom panel.

Figure 5 Top: LEED pattern of the surface carbide structure ($E = 40$ eV). Bottom: DF LEEM images ($E = 47$ eV, f.o.v.=4 µm) of three non–equivalent domains (A, B and C), related by an in–plane rotation of 120°. α and β indicate the two non–equivalent subdomains forming domain B, related by an in–plane rotation of ∼12°. The surface carbide was prepared by exposing the Re surface to a flux of C_2H_4 molecules (p= 2×10^{-7} mbar) and repeatedly annealing the sample up to 1200 K. This procedure allows allows a uniform carbide layer extending over the whole sample with no signs of GR formation.

Figure 6 (a) C 1*s* spectrum of the Re surface carbide; (b-c) High resolution Re $4f_{7/2}$ core level spectra, acquired at $h\nu = 200$ eV, at (b) normal and (c) grazing emission.

Figure 7 LEED line profile evolution of GR/Re(0001), recorded *in situ* during C_2H_4 CVD on Re(0001) through a series of heating/cooling cycles. (b) Sample temperature *vs* time during C_2H_4 CVD. (c) Intensity evolution of the (0,0) (red) and of the (0.92,0) moirè (blue) LEED spot

during GR formation on Re(0001). (d) Moirè LEED pattern of a high quality GR layer on Re(0001).

Figure 8 (a) DFT–calculated C−C nearest neighbour distance inside the moiré cell of GR/Re(0001). (b) Plot of the calculated C−C nearest neighbour distance *vs* C−Re distance. The colour scale in both (a) and (b) is proportional to the C−C bond length. (c) DFT–simulated moiré cell of GR/Re(0001) (only the first layer of the substrate is shown). (d) Calculated C 1*s* core level BEs *vs* C−Re distance, showing a monotonic dependence between the two quantities. The blue color scale reflects the atomic core level BEs.

Figure 9 Photoemission intensity evolution of the different C 1*s* spectral components during annealing of GR/Re(0001) from 1100 to 1240 K.

Figure 10 BF LEEM images (E=4 eV, f.o.v.: 4 µm) acquired during the annealing of GR/Re(0001) at increasing temperature (see insets in the figures). (a) GR-covered Re surface at the beginning of the experiment, showing a uniform grey shade; (b) carbide nucleation, accompanied by the appearance of dark spots at the steps and on the terraces; (c-e) expansion of the surface carbide phase; (f-g) thermally-induced bulk dissolution of the surface carbides (the bright halo around the dark spots is caused by the different work function of the clean and carburised regions of the substrate); (h) bare Re(0001) surface visible after C bulk dissolution.